ARCHIVE OF MECHANICAL ENGINEERING

DOI: 10.24425/ame.2025.186872 2025, Vol. 72, No. 4, pp. 715–740

Wuduan ZHAO [1], Wanjin GUO [2]

Adaptive parameters fusion regulation strategy of robotic polishing for unknown free-form surface

Received 29 March 2025, **Revised** 08 October 2025, **Accepted** 28 October 2025, **Published online** 26 November 2025

Keywords: adaptive parameter regulation, robotic polishing, material removal distribution, surface normal estimation, online trajectory generation

In response to the increasing demand for automation and compliance in robotic manufacturing, particularly in polishing applications, a novel trajectory generator has been developed to address the challenges associated with polishing diverse workpiece that lack prior geometric surface models. This generator utilizes a estimator for surface normal prediction of free-form surfaces in real time, integrating tool feed direction and reaction force to account for frictional interactions, thereby enabling dynamic regulation of subsequent trajectories. To achieve precise polishing control, a modified Material Removal Rate (MRR) distribution, derived from the estimated surface normal, is employed. Additionally, a model-predictive adaptive parameter fusion regulation strategy (APFRS) is introduced, which leverages the modified MRR to estimate material removal distribution and facilitates online adjustments to key parameters such as normal polishing force and feed rate. This ensures compliance with specified material removal depth requirements. Validation through numerical simulations and co-simulations using ADAMS and MATLAB/Simulink demonstrates the robustness of APFRS in adaptively regulating these parameters to maintain uniformity, thus enhancing the efficiency and adaptability of the polishing process for free-form workpiece without requiring complex, pre-defined trajectory planning.

✉ Wanjin GUO, email: guowanjin@chd.edu.cn

[1]School of Mechanical Engineering, Dalian University of Technology, Dalian, Liaoning, China.Email: zhaowudaun@mail.dlut.edu.cn

[2]Key Laboratory of Road Construction Technology and Equipment, Ministry of Education, Chang' an University, Xi'an, Shaanxi, China

1. Introduction

Enduring issues related to intelligent manufacturing, especially polishing in the industrial application, have drawn researchers' attention recently.There is a growing requirement for free-form optical components in communication, medical, and optoelectronic industries, along with escalating precision requirements and stricter demands on their processing capabilities[1–6]. The geometric complexity of free-form surfaces further exacerbates challenges and difficulties in precision manufacturing. As an important procedure of manufacturing processes, polishing demands high accuracy involving both positioning and polishing force of machining equipment. This significance becomes particularly pronounced when dealing with the intricate task of polishing free-form workpiece [7]. Traditionally, manual polishing has been characterized by labor-intensive efforts and inconsistent quality, rendering it unsuitable for human involvement due to the associated risks to workers' health (occupational disease) over prolonged periods in the polishing workshop [8]. Hence, equipment for high compliance and automation is imperative for the polishing process of free-form surface workpiece. To date, the utilization of industrial robots as a key component in polishing systems is a prevalent practice in manufacturing. Compared to computerized numerical control (CNC) machines, the merits of industrial robots are lower cost, lightweight, high flexibility and extensive integration capabilities with diverse end-effector and sensors. Consequently, robotic polishing systems can effectively and economically meet the stringent demands for polishing free-form surface workpiece, and make significant progress in liberating workers from injurious dust and noise [9].

According to the Preston material removal model, feed rate, spindle speed, dwell time and particularly polishing pressure act as primary factors in the polishing process, whereupon the stability and accuracy of polishing force applied in the normal direction of the workpiece surface plays a pivotal role since it dominates polishing pressure. This is due to the requirement that the drive direction of force actuator is exactly perpendicular to the surface of the workpiece [10]. Therefore, early works have delt with leveraging hybrid force/position control, i.e., impedance or admittance control, to achieve high-quality surface finishing through industrial robots [11–18]. These were based on a pre-defined path/trajectory generated by the CAD model of the workpiece utilizing the method as described in [19–21]. On the other hand, there are still some researchers who focus attention on controlling the relative position of the polishing tools with respect to the workpiece surface. One assumes that the contact between the polishing tool and the free-form workpiece surface is modeled as a tool central point (TCP) capable of sliding along the surface during the movement of polishing tool. Subsequently, the components of the contact force along the orthogonal coordinates obtained through the force/torque sensor can be employed to theoretically estimate the surface normal in frictionless contact [22–27]. Based on this prerequisite, a serial-parallel mechanism polishing machine that can polish workpiece efficiently can be developed,

however, the estimated errors of surface normal angle and normal polishing force are large [28]. In terms of polishing workpiece without prior geometric data, a passive end-effector fixed to a three-axis force is proposed, in spite of the fact that, because of vibrations and chatter, is cannot precisely perform measurement in real-time when acting in polishing or grinding machining [29]. Real-time estimation of the contact state between the polishing tool and the workpiece by predicting the surface normal direction of the workpiece is performed, however, it poses a challenge in ensuring the ultimate quality of finished workpiece [30]. Outstanding polishing efficiency can be achieved by integrating hybrid constraints with planning the feed rate and considering the polishing force. However, it leads to increasing complexity in preplanning the polishing process [31]. Generally, the normal surface estimation performed in the mentioned researches makes a significant impact on contact-intensive tasks, but the researchers turn a blind eye to the effect of friction in feeding. In the meantime, they neglect the direct feedback from the polishing tasks – final quality of the polished workpiece, which primarily depends on the material removal amount. Thus, this research focuses on how to conduct an accurate normal surface estimation and automatically modulate the material removal for reducing the surface roughness and improving the quality of the polished workpiece.

Without loss of generality, friction, which especially dominates the operation mechanism of polishing, is ubiquitous in contact-intensive tasks. However, friction in the feeding direction inevitably leads to measurement noise in normal vector estimation and adverse effects on the accuracy of material removal depth control in practical applications. At the same time, the final quality of polished workpiece is influenced by several factors associated with the uniformity and inconsistency of material removal depth in the polishing process. The material removal rate (MRR) is dominated by polishing pressure, feed rate, spindle speed, and dwell time, and notably, the polishing pressure is generated by contact force exerted on the unit area [32]. These factors collectively serve as quantitative criteria for material removal prediction. Moreover, when they are regulated separately and individually, the actual material removal depth may not be exactly in line with the desired value in real-time, leading to profile errors in the polished free-form workpiece [33]. Consequently, the guarantee of stability of the polishing pressure and the consistency of feed motion ensure the required polishing quality [34].

This paper presents a novel online trajectory generator comprising a friction-compensated estimator of the surface normal and a modified Preston material removal model, integrated with a model-predictive adaptive parameters fusion regulation strategy (APFRS). It is aimed to enhance the quality of robotic polishing of unknown free-form surfaces by dynamically optimizing polishing trajectories and adaptively regulating normal force and feed rate in real-time, in consequence, it allows achieving consistent high-quality finishes without reliance on prior CAD models. This method introduces an advance to the automation of robotic polishing, significantly reducing human intervention. Ultimately, co-simulations in ADAMS

and MATLAB/Simulink demonstrate the convergence of the surface normal to the actual vector, which is a development critical for the successful functioning of the proposed APFRS.

The article is organized as follows: In Section 1 we outline the related work in robotic polishing modeling. Section 2 exhibits the mechanical structure design, force controller of the end-effector, and trajectory generation; Section 3 discusses the theory behind the proposed APFRS; Section 4 presents several robotic polishing simulations on free-form surface workpiece; and Section 5 concludes the study.

2. Polishing trajectory estimation for unknown constraint surface

2.1. Mechanical structure and force controller

Industrial robots, essential in robotic systems, determine the spatial position and posture of the tool center point (TCP); however, achieving accurate force control for direct workpiece polishing remains challenging. A compliant end-effector with additional redundant degrees of freedom (DOF) addresses this issue by decoupling position/posture control from force control, which is a key research area. Designed for stable and accurate force control, the end-effector integrates a redundant DOF actuator with a spindle and movable platform, enabling floating polishing. An admittance controller further ensures robust and consistent normal polishing pressure on the workpiece surface.

2.1.1. Mechanical structure

A specially designed end-effector with a floating spindle, shown in Fig. 1, has been developed for compliant polishing, integrating a force/torque sensor at the flange of an industrial robot. This end-effector comprises a linear voice coil motor (LVCM) for accurate force control and a motorized spindle for rotational tool movement. The LVCM dynamically adjusts spindle stroke by modulating the coil current, realizes a telescoping motion of the polishing tool, and applies a controlled force to the workpiece with high accuracy. For the sake of consistency, we omit detailed explanation. The decoupled linear and rotational movements enhance flexibility, allowing adaptation to various workpiece geometries and materials. Controlled by the industrial robot to maintain optimal position and orientation, this end-effector design offers a robust solution for adaptable, precise robotic polishing, significantly improving system efficiency and polishing quality.

2.1.2. Normal force controller

Robotic polishing systems achieve high precision and effective contact handling by incorporating force controllers on the end-effector, such as proportional-integral-differential (PID), impedance, or admittance controllers, each suited to

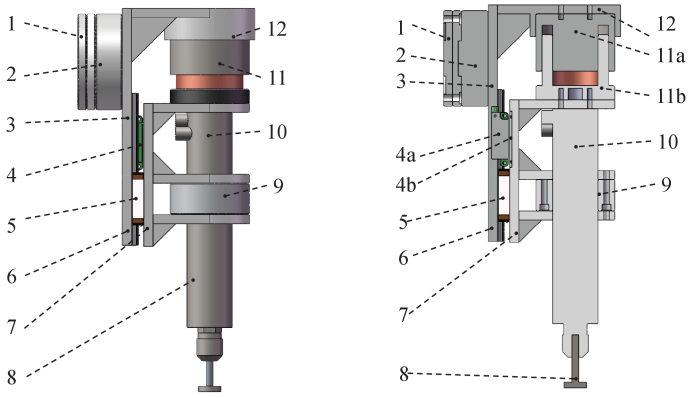

Fig. 1. Composition of the mechanical structure of the designed end-effector: (a) mechanical structure; (b) cross section view. 1 – connector I, 2 – force/torque sensor, 3 – support board of guide, 4 –linear encoder (4a – mover, 4b – stator), 5 – mover of guide, 6 – guide, 7 – moving platform, 8 – polishing tool, 9 – cylindrical fixture, 10 – spindle, 11 – LVCM (11a – stator of LVCM, 11b – mover of LVCM), 12 – support board of LVCM

specific applications. The admittance controller, noted for its compliance and stable position tracking, excels in force control during contact-intensive tasks, like polishing. Typically, it combines an inner PID-based position controller with a force compensator based on an impedance model, as illustrated in Fig. 2. Here, the force deviation F_d, defined as the difference between the expected force F_e and the actual normal polishing force F_n, serves as the input for the impedance model of admittance controller.

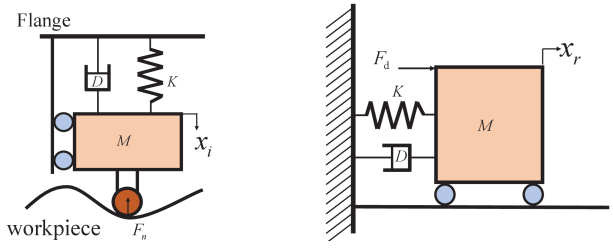

Fig. 2. Diagram of (a) position controller and (b) impedance model for admittance controller

Let's assume that the relationship between the deviation F_d and the elastic strain of the workpiece along the normal direction of the surface can be described by the second-order differential equation as

$$M\ddot{x} + D\dot{x} + Kx = F_d, \tag{1}$$

$$F_d = F_e - F_n. \tag{2}$$

Here, M, D and K denote the coefficients of the inertial, damping, and stiffness of the impedance model, respectively. The force compensation can be transformed into stroke compensation x_r for LVCM by applying the impedance model utilizing the Laplace transform to equation (1). Assuming a deviation $F_d(s) = A/s$, the steady-state error of normal force tracking is given by equation (4).

$$X_r(s) = \frac{F_d(s)}{Ms^2 + Ds + K}. \tag{3}$$

$$e_{ss} = \lim_{s\to 0} sX_r(s) = \lim_{s\to 0} \frac{s\frac{F_d(s)}{M}}{s^2 + \frac{D}{M}s + \frac{K}{M}} = \frac{A}{K}. \tag{4}$$

The outstanding tracking capability of the employed force controller is validated through theoretical analysis, demonstrating that under a deviation F_d, the error e_{ss} converges to a constant value, ensuring the stability of the interaction.

$$x_i = x_r + x_e - d_L, \tag{5}$$

where x_r, x_e and d_L represent the compensated stroke, the desired stroke and actual stroke of the LVCM, respectively.

2.1.3. Gravity compensation

The approaching direction of the spindle is defined as the extension direction from the rear end of the spindle along the axis towards the grinding tool. During the polishing process of free-form surface workpiece, industrial robots dynamically adjust the posture of the end-effector. When the approaching direction of the spindle deviates from the direction of gravity, as depicted in Fig. 3, it is essential to compensate for the gravitational effect on the output force of the LVCM of the

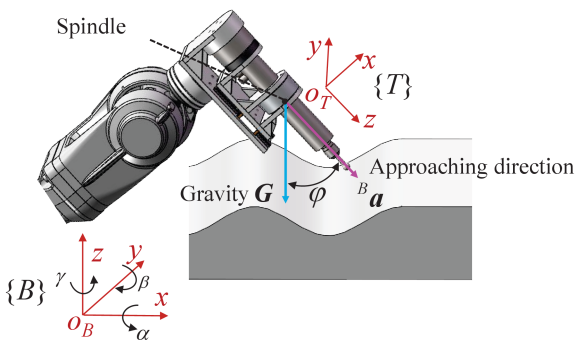

Fig. 3. Relationship between the direction of gravity and spindle

end-effector in real-time. This facilitates accurate control of the normal polishing force by the force controller.

In the virtual prototype, real-time acquisition of the tool coordinate system T orientation relative to the base coordinate system B is performed capturing roll (α), yaw (β), and pitch (γ) angles (RPY angles). Given the established transformation between RPY angles and the posture matrix, the posture matrix for the tool coordinate system T is derived from equation (6).

$$\boldsymbol{R} = \begin{bmatrix} \cos\alpha\cos\beta & \cos\alpha\sin\beta\sin\gamma - \sin\alpha\sin\gamma & \cos\alpha\sin\beta\cos\gamma + \sin\alpha\sin\gamma \\ \sin\alpha\cos\beta & \sin\alpha\sin\beta\sin\gamma + \cos\alpha\cos\gamma & \sin\alpha\sin\beta\cos\gamma + \cos\alpha\sin\gamma \\ -\sin\beta & \cos\beta\sin\gamma & \cos\beta\cos\gamma \end{bmatrix} = \begin{bmatrix} \boldsymbol{n} & \boldsymbol{o} & \boldsymbol{a} \end{bmatrix} \tag{6}$$

Considering that the spindle's approaching direction aligns with the z-axis of the tool coordinate system T, the unit vector representing the spindle axis direction can be inferred directly. Furthermore, the angle between the unit gravity vector and the unit vector of the spindle approaching direction in the reference coordinate system B can be determined by equation (7):

$$\phi = \arccos\left(\frac{\boldsymbol{a}\cdot\boldsymbol{G}}{||\boldsymbol{a}||\cdot||\boldsymbol{G}||}\right), \quad \boldsymbol{G} = [0, 0, 1]. \tag{7}$$

Here, ϕ is available in the range of 0° to 180°, $\boldsymbol{G}$ represents the gravity direction vector. According to the angle and the mass of the spindle and the moving platform M_p, the compensatory force of LVCM can be obtained by equation (8).

$$F_g = M_p \cos\phi. \tag{8}$$

Subsequently, gravity compensation is implemented for normal polishing force control to mitigate the influence of the spindle and the moving platform's gravity. The block diagram of the force controller with gravity compensation for the end-effector is constructed as depicted in Fig. 4.

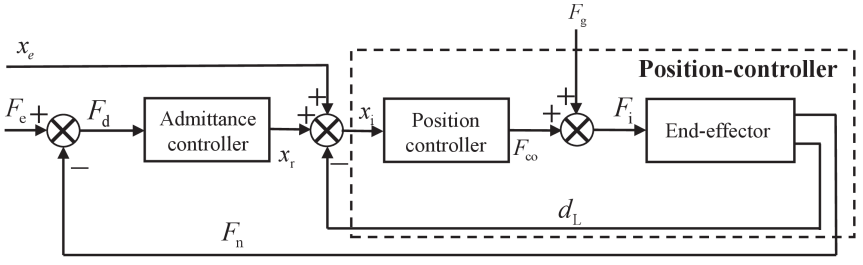

Fig. 4. Block diagram of normal polishing force controller with gravity compensation

2.2. Surface normal vector estimation

Extensive research has demonstrated that the polishing force between the tool and workpiece is a critical factor in determining both the quality and efficiency of the polishing process [35–38]. To achieve precise polishing, it is essential for the polishing force to be oriented perpendicularly to the workpiece surface, which ensures accurate normal force control. However, accurately estimating the normal vector for unknown constraint surface without prior measurement through precise instrumentation presents a significant challenge. This section addresses the development of a normal vector estimation method for unknown constraint surface, utilizing the feed direction and reaction force between the TCP and the workpiece surface. Based on the estimated normal vector, the posture and position for subsequent cycles are determined, with a trajectory generator introduced for trajectory planning through linear and quaternion interpolation.

2.2.1. Definition of limitations

Given the inherent difficulty in accurately defining the description of constraint surfaces on the workpiece, a more advantageous approach would be to implement the control strategy without necessitating an overly explicit constraint. To clarify the control strategy, we establish the following prerequisites:

a) Firstly, it is imperative that the minimum curvature radius of the workpiece surface surpasses the length of the end-effector. Non-compliance with this condition may result in interference between the end-effector and the workpiece surface, hindering the posture adjustment of the approaching direction of the polishing spindle.
b) While the measurable feedback force from a constraint surface and the position of TCP in 3D space are critical factors to consider, the torque is intentionally disregarded because of its negligible impact on surface normal vector estimation. As a result, 3D force vectors are utilized to represent the measured force $\boldsymbol{f}_c$ and the position of TCP $\boldsymbol{P}(t)$.
c) Furthermore, a virtual constraint plane denoted as Q is introduced to predefine specific limitations on the polishing trajectory before the polishing process begins [39], as depicted in Fig. 5. The explicit definition of plane Q is established as follows:

$$\mathrm{Q}(\boldsymbol{\varepsilon}) = 0, \tag{9}$$

where $\boldsymbol{\varepsilon}$ represents the unit normal vector of plane Q in Fig. 5. The specified trajectory indicates that TCP follows the intersection line between plane Q and the constraint surface, a determination primarily governed by plane Q. In the same coordinate system, if plane Q is parallel to the base plane (XoY , YoZ or XoZ), one of the X, Y, or Z components of the coordinate of the polishing trajectory is constrained to zero.

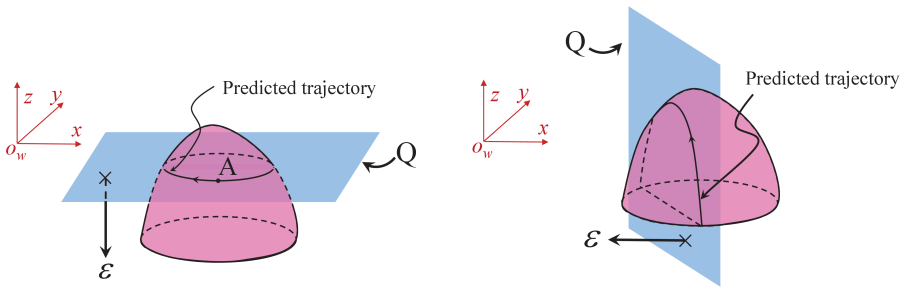

(a) case 1 (b) case 2

Fig. 5. Virtual constraint surfaces in experiments [39], (a) case 1: the plane Q is parallel to XoY, (b) case 2: the plane Q is perpendicular to XoY

2.2.2. Normal vector estimator

Let's assume that TCP affixed to the end of the end-effector is traversing the constraint surface along the intersection line between the constraint surface (workpiece) and the virtual constraint plane Q. Let $\Delta \boldsymbol{P}$ be the vector originating from the current point to the previous neighboring point on its trajectory within the time interval Δt, Then, $\Delta \boldsymbol{P} = \boldsymbol{P}(t) - \boldsymbol{P}(t - \Delta t)$. We consider the normalized $\Delta \boldsymbol{P}$ as the estimated feed direction $\boldsymbol{\upsilon} = \dfrac{||\Delta \boldsymbol{P}||}{\Delta t}$, representing the current tangent vector of the contact point trajectory that can describe the local contour of the constraint surface. Assuming the actual normal vector and the estimated normal vector of the constraint surface are denoted as $\boldsymbol{u}_n$ and $\hat{\boldsymbol{u}}_n$ respectively, one can theoretically assert that the feed direction $\boldsymbol{\upsilon}$ is perpendicular to the vector $\boldsymbol{u}_n$. Thus, a virtual plane G that is perpendicular to the vector $\boldsymbol{\upsilon}$ and intersects with the current tool position $\boldsymbol{P}(t)$ is established. It is evident that the vector $\boldsymbol{u}_n$ lies within the plane G.

Utilizing a force/torque sensor to measure the contact force, denoted as $\boldsymbol{f}_c$, exerted by the TCP on the surface, the surface normal is estimated leveraging method described above. This estimation is achieved by considering the force vector opposite to that applied by TCP, as illustrated in Fig. 6. The resulting calculation ensures that the approaching direction of the polishing spindle remains perpendicular to the surface while moving along the intersection line. As stated by the law of action and reaction forces, the direction of the reaction force $\tilde{\boldsymbol{f}}_c$ from the constraint surface typically aligns with the estimated normal vector $\hat{\boldsymbol{u}}_n$. The estimated normal vector is computed by $\hat{\boldsymbol{u}}_n = \dfrac{\tilde{\boldsymbol{f}}_c}{||\tilde{\boldsymbol{f}}_c||}$.

Nevertheless, in practical polishing processes, the friction force $\boldsymbol{f}_r$ consistently emerges and constitutes a significant portion of $\boldsymbol{f}_c$. Considering that $\boldsymbol{f}_r$ operates in the direction opposite to the advancement of TCP, we denote $\boldsymbol{f}_r$ as $\boldsymbol{f}_r = (\boldsymbol{f}_c \cdot \boldsymbol{\upsilon})\boldsymbol{\upsilon}$, which exhibits the relationship depicted in Fig. 6. Hence, the reaction force $\tilde{\boldsymbol{f}}_c$

can be computed using $\tilde{\boldsymbol{f}}_c = \boldsymbol{f}_c - \boldsymbol{f}_r$. Subsequently, we obtain a solution for the estimated normal vector as

$$\hat{\boldsymbol{u}}_n = \frac{\boldsymbol{f}_c - (\boldsymbol{f}_c \cdot \boldsymbol{v})\boldsymbol{v}}{||\boldsymbol{f}_c - (\boldsymbol{f}_c \cdot \boldsymbol{v})\boldsymbol{v}||}. \tag{10}$$

Defining the virtual constraint plane Q is essential to ensure continuous traversal of the contact point between the polishing tool and workpiece surface. To achieve this, a posture control axis and a position control axis are designated for the constrained workpiece surface. The posture control axis, represented by vector $\boldsymbol{a}$, is oriented consistently opposite to the surface normal vector $\boldsymbol{u}_n$, keeping the approach direction of the spindle perpendicular to the tangent plane at the contact point. Since $\boldsymbol{u}_n$ is unknown, the estimated normal vector $\hat{\boldsymbol{u}}_n$ is used as an approximation, yielding $\boldsymbol{a} = -\hat{\boldsymbol{u}}_n$

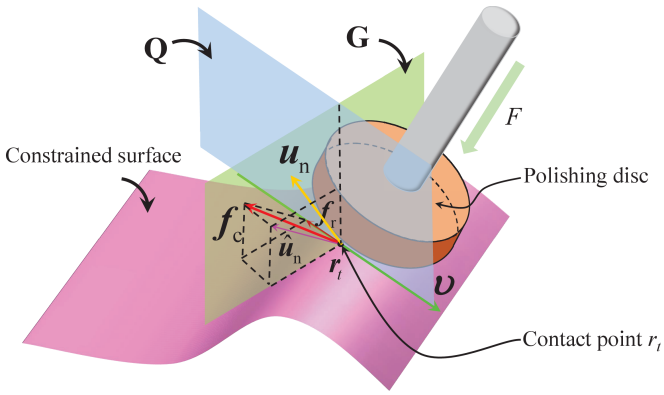

Fig. 6. Geometric relationship among the polishing tool, measured contact force, feed direction, and estimated surface normal

The position control axis is defined as the vector $\boldsymbol{n}$, which serves as a guide for forward feeding to predefine the polishing trajectory that is determined by the virtual constraint plane Q and the normal vector of the constraint surface. Accordingly, the vector $\boldsymbol{n}$ is determined by the vector $\boldsymbol{\varepsilon}$ and vector $\boldsymbol{a}$ can be calculated by $\boldsymbol{n} = \dfrac{\boldsymbol{\varepsilon} \times \boldsymbol{a}}{||\boldsymbol{\varepsilon} \times \boldsymbol{a}||}$, where $\times$ represents the product of vectors. While vector $\boldsymbol{n}$ may not be parallel to the virtual constraint plane Q because of position trajectory errors, it remains normal to vector $\boldsymbol{a}$. Consequently, we establish a right-hand coordinate system, denoted as Σ_t to describe the tool posture. The direction perpendicular to this system is referred to as $\boldsymbol{o} = \boldsymbol{a} \times \boldsymbol{n}$. Here, vector $\boldsymbol{n}$, $\boldsymbol{o}$ and $\boldsymbol{a}$ represent the x, y and z axis of coordinate system Σ_t respectively. Vectors $\boldsymbol{n}$ and $\boldsymbol{o}$ represent the position control directions, where $\boldsymbol{a}$ specifically serves as the posture control direction, also referred to as the force control direction. The matrix $\boldsymbol{R}(t + \Delta t) = [\boldsymbol{n} \quad \boldsymbol{o} \quad \boldsymbol{a}]$ is employed to characterize the posture of the coordinate system Σ_t.

As mentioned above, the surface normal vector is estimated and the desired posture for the tool coordinate system Σ_t is acquired. The approach direction of the spindle can be adaptively regulated according to the desired posture; achieving fully automated polishing is contingent upon the implementation of a positional control strategy in the subsequent phase.

2.3. Position derivation of subsequent period

The position control axis $\boldsymbol{n}$ serves as the guiding factor for the polishing process. The position of the subsequent period can be determined by advancing along the feed guidance vector. Assuming that the contour of the surface can be approximated by multiple micro-element lines, the position vector of the subsequent period can be expressed as equation (11).

$$\boldsymbol{P}(t+\Delta t) = \boldsymbol{P}(t) + \mu \boldsymbol{n}. \tag{11}$$

Clearly, $\boldsymbol{n}$ and μ represent the estimated feed direction and polishing feed rate of the subsequent period respectively. A homogeneous coordinate $\boldsymbol{T}(t)$ is formulated to represent both the position and posture of TCP coordinate system simultaneously

$$\boldsymbol{T}(t) = \begin{bmatrix} \boldsymbol{n}_t & \boldsymbol{o}_t & \boldsymbol{a}_t & \boldsymbol{P}(t) \\ 0 & 0 & 0 & 1 \end{bmatrix} = \begin{bmatrix} \boldsymbol{R}(t) & \boldsymbol{P}(t) \\ \boldsymbol{0} & 1 \end{bmatrix}. \tag{12}$$

As a result, the desired posture and position of TCP in the subsequent period can be represented as

$$\boldsymbol{T}(t+\Delta t) = \begin{bmatrix} \boldsymbol{R}(t+\Delta t) & \boldsymbol{P}(t+\Delta t) \\ \boldsymbol{0} & 1 \end{bmatrix}. \tag{13}$$

2.4. Trajectory generator based on position/posture estimation

The homogeneous coordinates of the TCP coordinate system can be obtained through the inverse kinematic algorithm, while the joint angles of the robot may be intractable near the singular points. Hence, trajectory planning is demanded between two neighbor periods. To avoid intricate computation and the Gimbal Lock issue, linear interpolation in Cartesian and spherical linear interpolation(SLERP) in quaternion space is separately utilized to generate the intermediate position/posture between two adjacent periods [40]. The number of interpolated points is set to K, it yields middle position and posture by equation (14) and (15), respectively.

$$\boldsymbol{P}_m = \boldsymbol{P}(t) + \frac{(K-j)}{K}\mu \boldsymbol{n}, m = 1, 2, ..., K, \tag{14}$$

$$\begin{aligned}
\boldsymbol{Q}(t) &= R2quat(\boldsymbol{R}(t)),\\
\boldsymbol{Q}(t+\Delta t) &= R2quat(\boldsymbol{R}(t+\Delta t)),\\
\boldsymbol{Q}_m &= \frac{\sin(1-\frac{(K-j)}{K})}{\sin(\alpha)}\boldsymbol{Q}(t) + \frac{\frac{(K-j)}{K}\alpha}{\sin(\alpha)},\\
m &= 1, 2, ..., K,\\
\alpha &= \arccos(\boldsymbol{Q}(t)\cdot\boldsymbol{Q}(t+\Delta t)),
\end{aligned} \tag{15}$$

where $R2quat$ is the function for transforming the posture matrix to quaternion. Accordingly, only starting points and virtual constraint plane Q are required to implement a full-automatic polishing process by utilizing the proposed method, theoretically.

3. Adaptive parameters fusion regulation strategy in polishing

To ensure the finishing requirement of the workpiece, it is crucial to maintain the quality of the robotic polishing process, which directly involves the regulation of the material removal procedure. Researchers have developed various models to precisely quantify the material removal depth. The primary objective in robotic polishing is to meticulously control the removal depth of the workpiece at each position along a specific trajectory, following the contour of the workpiece [41]. According to Preston's assumption, a material removal model is formulated as a canonical model rooted in Hertzian contact theory [42], commonly referred to as the Preston material removal model, which is expressed as:

$$h_t(x,y) = \frac{\mathrm{d}h(x,y)}{\mathrm{d}t} = K_p \cdot p(x,y) \cdot |\boldsymbol{v}(x,y)|, \tag{16}$$

where $h_t(x,y)$ is the material removal rate at the polishing contact point $\boldsymbol{r}(t)$ on the constraint surface of the finished workpiece, K_p denotes the Preston coefficient, parameters related to the properties of tool and workpiece, including Poisson's ratio and Young's modulus of the workpiece and the grinding tool, and the size of the tool, etc. In equation (16), $\frac{\mathrm{d}}{\mathrm{d}t}(\cdot)$ denotes the time derivative of a distribution. For instance, it may be influenced by factors such as the granularity of the polishing tool (disc). Here, $\boldsymbol{v}(x,y)$ and $p(x,y)$ symbolize the sliding velocity and polishing pressure of the contact point, respectively, at the contact point $\boldsymbol{P}(t)$ between the polishing tool and the workpiece surface.

3.1. Modified material removal distribution

According to the preceding analysis, equation (16) reveals that the principle that the material removal rate is exclusively influenced by the polishing pressure $p(x,y)$ when the sliding velocity $\boldsymbol{v}(x,y)$ remains constant, and vice versa.

Achieving uniform and consistent material removal requires stable and simultaneous control of both $p(x, y)$ and $\boldsymbol{v}(x, y)$. However, synchronously regulating $p(x, y)$ and $\boldsymbol{v}(x, y)$ poses a formidable challenge. Furthermore, maintaining a constant polishing pressure or feed rate may not always be feasible in the case of various working conditions, particularly when dealing with workpiece featuring free-form surfaces. To achieve the ultimate goal of supervising and controlling material removal amount during the polishing process, considering a fixed product of $p(x, y)$ and $\boldsymbol{v}(x, y)$ emerges as a practical approach, as outlined in equation (16).

According to the estimation of the surface normal vector, we assume that the direction of the polishing force consistently aligns parallel to the normal vector of the constraint surface, and the contact regions for the workpiece are considered approximately equivalent to the bottom surface of the polishing tool. The polishing pressure is then determined as follows [43]:

$$p(x, y) = \frac{F_n}{\pi R^2}\sqrt{1 - \left(\frac{x}{R}\right)^2 - \left(\frac{y}{R}\right)^2}, \tag{17}$$

where R represents the radius of the tool bottom surface area, and F_n signifies the normal polishing force exerted by the end-effector. The sliding velocity $\boldsymbol{v}(x, y)$ of the inner point E comprises the disc sliding velocity $\boldsymbol{v}_s$ and translation velocity $\boldsymbol{v}_t = \mu \boldsymbol{n}$ in the XoY coordinates in Fig. 7. In this frame, the x-axis is parallel to the translation velocity $\boldsymbol{v}_t$, the y-axis is perpendicular to the x-axis, and the z-axis is determined by the right-hand coordinate system, as illustrated in Fig. 7. The point O denotes the center-point of the tool bottom surface, θ represents the angle between OE and the positive direction of the x-axis, $\theta = \arctan\frac{y}{x}$, $\cos\theta = \frac{x}{\sqrt{x^2 + y^2}}$, $\sin\theta = \frac{y}{\sqrt{x^2 + y^2}}$.

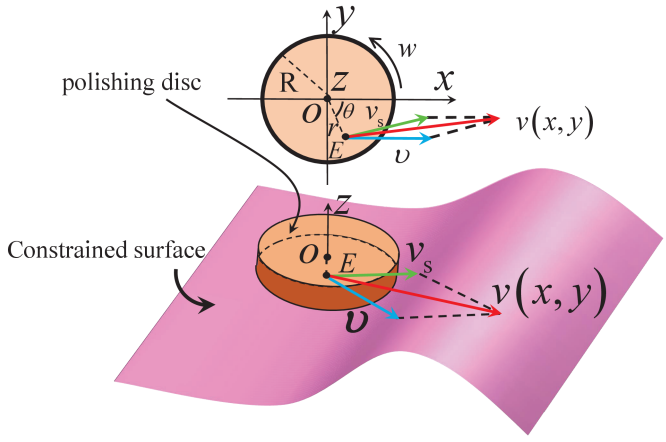

Fig. 7. Correlation between the sliding velocity, disc sliding speed and translation velocity

Moreover, the direction of the normal polishing force deviates from the surface normal vector when the contact state changes, as a result, the contact area will not be equivalent to the bottom surface of the polishing tool. As seen in Fig. 8, the direction of reaction force can vaguely reflect the contact state, it can rather be considered as the position deviation of the central point of the contact area in tool coordinate system E. Coefficients of deviation η_x and η_y in the x and y direction of tool coordinate system E are defined to describe the deviation of central point of contact area, which is calculated by equation (18) using $\boldsymbol{n}_t$, $\boldsymbol{o}_t$ and estimated normal vector $\hat{\boldsymbol{u}}_n$.

$$\begin{cases} \eta_x = \boldsymbol{n}_t \cdot \hat{\boldsymbol{u}}_n, \\ \eta_y = \boldsymbol{o}_t \cdot \hat{\boldsymbol{u}}_n. \end{cases} \tag{18}$$

Subsequently, the pressure distribution after deviation of the contact area central point is yielded underlying equation (17) and coefficients of deviation, which are leveraged to adjust polishing force control process.

$$p(x, y, \eta_x, \eta_y) = \frac{F_n}{\pi R^2} \sqrt{1 - \left(\frac{x - \eta_x R}{R}\right)^2 - \left(\frac{y - \eta_y}{R}\right)^2}. \tag{19}$$

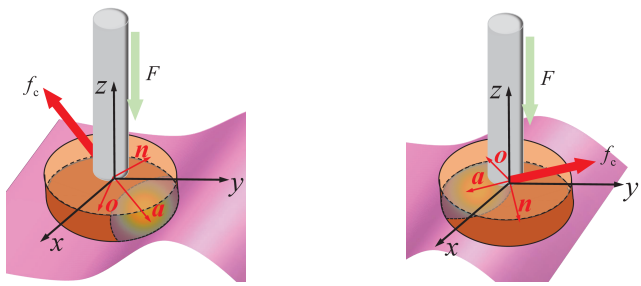

(a) pose 1 (b) pose 2

Fig. 8. Different contact state at two poses, (a) pose 1: positive surface curvature, (b) pose 2: negative surface curvature

We denote the tool angular velocity as ω, the spindle speed as $n = 60 \cdot \frac{\omega}{2\pi}$, and the disc sliding velocity can be calculated by $\boldsymbol{v}_s(x, y) = \boldsymbol{\omega} \times \boldsymbol{r}$, where $\boldsymbol{r}$ is the distance between center-point O and inner-point E of the tool bottom surface, $|\boldsymbol{r}| = \sqrt{x^2 + y^2}$. Afterward, the translation velocity at the inner point E is obtained through vector addition between $\boldsymbol{v}_s(x, y)$ and μ. We can describe the sliding velocity of E as $\boldsymbol{v}(x, y) = \boldsymbol{v}_s(x, y) + \boldsymbol{v}_t$, whose L2 norm is expressed by equation (20)

$$|\boldsymbol{v}(x,y)| = \sqrt{(|\boldsymbol{\omega}| \cdot x)^2 + (\mu - |\boldsymbol{\omega}| \cdot y)^2}. \tag{20}$$

To make explicit formulation, a generalized vector ξ is introduced, which is expressed as $\xi = [F_n \ \mu \ n \ T \ \eta_x \ \eta_y]$. By substituting equation (17) and (20) into (16), the material removal rate is derived as:

$$h_t(x,y,\xi) = \frac{K_p F_n}{\pi^2 R^3} \sqrt{\left((|\boldsymbol{\omega} \cdot x|)^2 + (\mu - |\boldsymbol{\omega}| \cdot y)\right)^2} \sqrt{R^2 - (x - \eta_x R)^2 - (y - \eta_y)^2} \tag{21}$$

According to the Preston equation, the modified MMR distribution, denoted as $h(x,y,\xi)$, is calculated through the integral of $h_t(x,y,\xi)$ with respect to the dwell time T, and is expressed as follows:

$$\begin{aligned} h(x,y,\xi) &= \int_0^T h_t(x,y,\xi)\,\mathrm{d}t \\ &= \frac{K_p F_n T}{\pi^2 R^3} \sqrt{\left((|\boldsymbol{\omega} \cdot x|)^2 + (\mu - |\boldsymbol{\omega}| \cdot y)\right)^2} \sqrt{R^2 - (x - \eta_x R)^2 - (y - \eta_y)^2} \end{aligned} \tag{22}$$

The speed ratio is symbolized by $\lambda = n:\mu$ to represent the relationship between the spindle speed n and the feed rate μ. The spindle speed n, radius of disc R and normal polishing force F_n are set to 2000 r/min, 15 mm and 30 N, respectively. Assuming that we don't consider the Preston coefficient K_p, which is determined by experimental calibrations and is mostly invariant, the varying values of parameters in $h_t(x,y,\xi)$ are presented in Table 1.

Table 1. Parameters of the MRR distribution

No	feed rate μ [mm/s]	Speed ratio λ	η_x	η_y	Estimated normal vector $\hat{\boldsymbol{u}}_n$
1	0.1	20000:1	0	0	[0,0,1]
2	0.5	4000:1			
3	2	1000:1			
4	2.5	800:1			
5	2.5	800:1	0.7071	0	[1,0,1]
7			0	0.7071	[0,1,1]
8			0.5774	0.5774	[1,1,1]

Subsequently, numerical calculations are performed by substituting different estimated normal vectors $\hat{\boldsymbol{u}}_n$ into equation (18), which yields separate η_x and η_y, and the shape of the modified MRR distribution with various speed ratios $\lambda(n{:}\mu)$ is illustrated in Fig. 9.

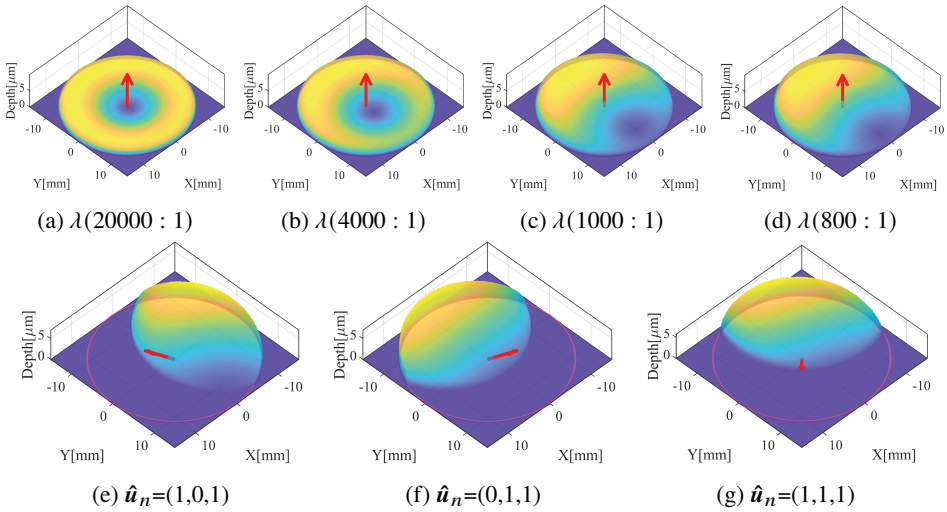

(a) $\lambda(20000:1)$ (b) $\lambda(4000:1)$ (c) $\lambda(1000:1)$ (d) $\lambda(800:1)$

(e) $\hat{\boldsymbol{u}}_n$=(1,0,1) (f) $\hat{\boldsymbol{u}}_n$=(0,1,1) (g) $\hat{\boldsymbol{u}}_n$=(1,1,1)

Fig. 9. MRR distribution under specific speed ratio λ and different estimated normal vectors $\hat{\boldsymbol{u}}_n$ (red arrow) in tool coordinate E

Explicitly, the modified MRR distribution is convex when the speed ratio is low but becomes concave as the speed exceeds a specific value, which is attributed to the dominance of the feed rate μ in the polishing process when μ is relatively larger, whereas the spindle speed governs the material removal amount if n is much higher. Hence, when λ is within the range of 800:1 to 1000:1, the distribution is predominantly successive. Nevertheless, a singularity emerges (as indicated by the convex region in Fig. 9) in the distribution when λ is higher than 1000:1. Eventually, the optimal value for λ falls within the range of 800 to 1000 within numerical simulation. Correspondingly, the optimal feed rate is confined to the range of 2 mm/s to 2.5 mm/s when n equals 2000 r/min.

3.2. Adaptive Parameters Fusion Regulation Strategy (APFRS)

Vibrations and chatters in the polishing process lead to variability and instability in material removal, posing challenges in ensuring the finishing quality of polished workpiece. To address this issue, we propose a model-predictive adaptive parameters fusion regulation strategy (APFRS) that integrates multiple factors, which treats the complexities of multi-target control as a single-target optimization problem.

Supposing that the reference material removal amount, the initial normal polishing force and feed rate are given, if the contact state varies during the control period due to changes in posture and position by the trajectory generator, the normal polishing force inevitably deviates from the reference value. Based on the analysis, the normal polishing force F_n and feed rate μ are considered in the proposed strategy. Hence, for the purpose of monitoring the contact state, κ is introduced as

the product of $\boldsymbol{a}$ and $\boldsymbol{a}_t$. So far, the normal of free-form surface alters relatively steadily if $\kappa \approx 1$, and surface curvature variation occurs suddenly when κ largely deviates from 1. Furthermore, the magnitude of deviation is determined by the distance between κ and 1 (i.e., $(\kappa - 1)^2$). To ensure the reference material removal in the polishing process, the feed rate needs to be updated, given that the maximum and minimum of the feed rate and the reference normal polishing force are defined as $\mu_{\min}$, $\mu_{\max}$, $F_{\min}$ and $F_{\max}$, then the updated law of feed rate and polishing force is calculated by equation (23).

$$\begin{cases} \mu_m = \mu_{\min} + (1 - \dfrac{(\kappa - 1)^2}{4})(\mu_{\max} - \mu_{\min}), \\ F_m = F_{\min} + (1 - \dfrac{(\kappa - 1)^2}{4})(F_{\max} - F_{\min}). \end{cases} \tag{23}$$

Here, substituting the κ to equation (23), yields the regulated μ_m, alternatively the regulated F_m, thus the other dependent variable can be computed by equation (22) since the reference material removal depth is restricted. Afterwards, the theoretical material removal depth is guaranteed, which ensures the uniformity and consistency of workpiece would be accomplished definitely. η_x, η_y and κ are identified as hyper-parameters of APFRS. The overall framework is depicted in Fig. 10. The components of the proposed APFRS are specifically introduced as follows:

a) Normal force controller: An admittance controller (as elaborated in Fig. 4) is employed to track the reference normal polishing force for the sake of the requirement of consistent and uniform polishing pressure.

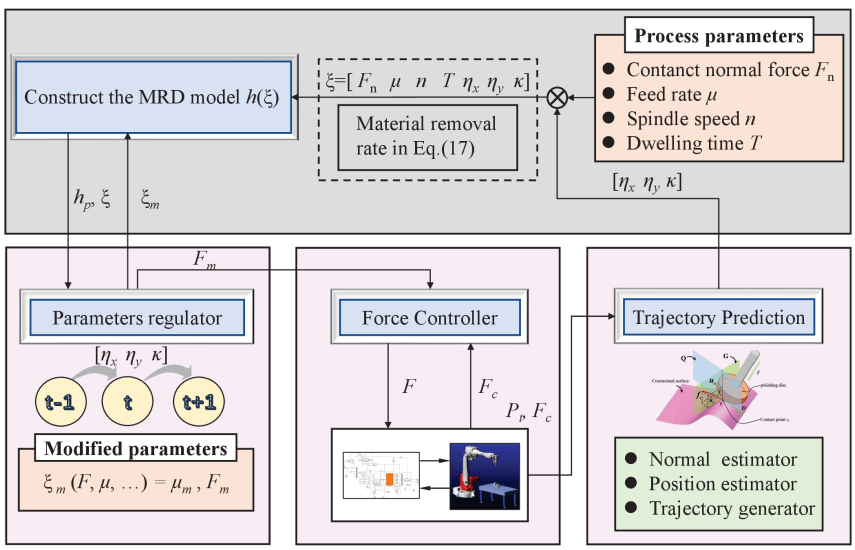

Fig. 10. Adaptive parameters fusion regulation strategy (APFRS) for robotic polishing

b) Trajectory estimator: The normal vector and the position of the subsequent period are estimated according to equation (9) to (13).
c) Removal predictor: Material removal depth distribution h_p is predicted by the proposed modified MRR distribution (refer to equation (22)) underlying the given parameters from generalized vector ξ.
d) Parameters regulator: The parameters μ_m and F_m in the generalized vector ξ are updated for the subsequent polishing period according to κ, which directly determines the flatness and quality of polishing process.

Additionally, we conducted polishing simulation to validate the effectiveness of the proposed method as seen in Section 4.

4. Simulation validation

To verify the effectiveness and adaptability of the proposed APFRS method without prior geometric data, in this section, robotic polishing simulation is carried out underlying a virtual prototype of a robotic system, which is equipped with the proposed end-effector within a co-simulation environment at ADAMS and MATLAB/Simulink, for performing simultaneously constant force and adaptive normal vector tracking of the free-form surface workpiece. The virtual prototype comprises an industrial robot with six degrees of freedom (Model: ABB IRB 2600), the proposed end-effector with a floating telescoping part attached at the end of the robotic arm and a working table. A disc with a diameter of 15 mm and thickness of 10mm is attached at the end tip of the spindle. The telescoping displacement of LVCM, spindle speed and feed rate are controlled by the MATLAB/Simulink, and the surface of free-form workpiece is modeled by SolidWorks, the material of workpiece is Aluminum 6061. The aim of the simulation settings is to validate the effectiveness of the proposed APFRS. The employed virtual prototype of the robotic polishing system is built as shown in Fig. 11.

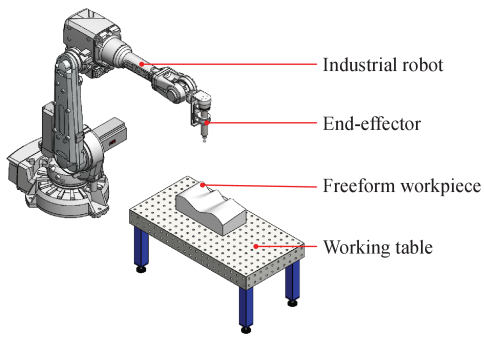

Fig. 11. Virtual prototype of a robotic polishing system

4.1. Procedures for implementing co-simulation in ADAMS-MATLAB/Simulink

The development and implementation of the virtual robotic polishing system involve a systematic integration of finite element modeling, multi-body dynamics simulation, and control system design. The overall procedure is summarized as follows:

a) The flexible body (finite element model)of free-form workpiece is exported from ANSYS Workbench as a modal neutral file (MNF). The parameters of contact force property are configured as shown in Table 2.
b) Construction and configuration of robotic polishing system virtual prototype is conducted in ADAMS, including importing the MNF, and exporting the mechanical system model to MATLAB/Simulink from ADAMS plug-ins.
c) Designing and building the trajectory generator and the APFRS in MATLAB/Simulink
d) Integrating and performing the virtual robotic polishing system and collecting generated data for analysis.

Table 2. Parameters of contact force property in ADAMS

Parameters	Value
Stiffness	35000
Force exponent	28
Damping	1.5
Penetration depth	0.1
Static coefficient	0.25
Dynamic coefficient	0.2
Stiction transition	0.1
Friction transition	10

4.2. Simulation initialization

The polishing process is segmented into three working phases, which are depicted as the approaching stage (*Phase* 1), the polishing stage (*Phase* 2) and the leaving stage (*Phase* 3), respectively. Each description of the working phases is shown as follow:

a) *Phase* 1:The fundamental requirement for APFRS is that the polishing disc is in contact with the workpiece, because the contact force signal is indispensable. Accordingly, the contact between tool and workpiece is required during *Phase* 1 initially. Simultaneously, the starting point is denoted as A while contact interaction occurs. The polishing disc moves from the initial position to the point getting in touch with the workpiece, confirming that

the force/torque sensor can detect the effective signal, which provides calculation foundations for APFRS. Generally, *Phase* 1 executes the simplest task such as moving along a straight line or circle, but plays a pivotal part in the overall task.

b) *Phase* 2: The proposed APFRS is completely implemented in this phase, acting at full capacity within the global polishing procedure. A stable and flexible force-related signal between TCP and the workpiece is acquired through the fine-tuned force controller. It allows performing accurate estimation of the surface normal and regulation of the parameters, which ensures the flatness and smoothness of workpiece finishing in the polishing process, controlling the depth of the reference material removal.

c) *Phase* 3: The contact interaction between the tool and workpiece must be terminated once the position of the tool surpass the prescribed polishing range, then the robotic polishing system would keep the end-effector away from the workpiece to avoid a potential collision.

For precise monitoring of the polishing process, it is essential to determine the starting- and ending-point *A* and *B*, respectively. Consequently, the normal vector of virtual constraint plane Q is designated and the straight line path with the starting-point A(1000, 50) and the ending-point B(1400, -50) in XoY is set, as depicted in Fig. 12. Here, the path planning of TCP is implemented primarily in 2D coordinates XoY (the predefined path can be planned in a different plane, according to various polishing tasks), which implies that the x and y component of TCP is predefined, and the z component of the traversed trajectory will be calculated by equation (13) in real-time during *Phase* 2. Afterward, the traversed trajectory of the polishing disc is along the projection of the predefined path on the workpiece surface.

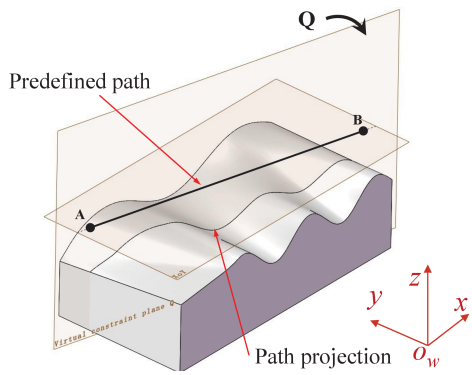

Fig. 12. Projection of predefined path on the workpiece surface

4.3. Robotic polishing simulation

With the aim of the verified APFRS, the predefined path planning for polishing the workpiece is conducted as stated above. It guarantees that there are variations in surface normals along the path, and ensures the continuity of interaction between the tool and the workpiece, which satisfy the prerequisite of trajectory estimator, providing a fairly well accuracy. To perform polishing operations on the workpiece along the predefined path with pose and parameters regulation underlying the proposed strategy, the robotic polishing simulation is carried out in the case of a spindle speed of 800 rpm and a feed rate of 1 mm/s, with different reference normal polishing forces of 20 N, 30 N and 40 N, under admittance and PID controller, respectively. The contact force is filtered by a high-frequency second-order Butterworth low-pass filter with a cutoff frequency of 17 Hz and sampling interval of 5 ms. The inertial, damping and stiffness coefficient of admittance parameters are assumed as: M=70 kg, D=120 N m/s, K=10 N/m, and the parameters of PID controller are: Kp=1.4, Kd=0.001, Ki=0.25. The angle between the estimated surface normal and the raw surface normal can indicate the prediction error of surface normal estimator [15].

During the polishing process simulation, the normal polishing force and force error, the telescoping displacement, the regulated normal polishing force and the angle error of estimated surface normal vector under PID and admittance controller are elaborated in Fig. 13.

The admittance controller with gravity compensation, applied instead of PID controller, performs an excellent task of tracking the reference force and keeping low the telescoping displacement as shown in Fig. 13, where the maximum error of the normal polishing force is only 1.9 N under different reference forces with a mean error within 0.53 N. The maximum of angle error lies in range of 0.01° to 1.33°, which means that the approaching direction of spindle is approximately the same as the direction of the raw surface normal vector. The above result reveals that the proposed APRFS has a remarkable capability in trakcing synchronically toward normal polishing force and surface normal vector. At the same time, the regulation of the reference normal polishing force assures that the material removal rate is constant in real-time and the lower telescoping displacement keeps the LVCM always in the best state of stable and controllable output range.

As shown in previous analysis, the proposed APFRS can be regarded as an optimization issue, which aims to confirm consistency and uniformity of material removal depth in the polishing procedure. Hence, the fine-tuned hyper-parameters(F_e, μ, n, T) are required to attain the prescribed target. These parameters include spindle speed n, feed rate μ, polishing pressure $p(x, y)$, and dwell time T. The speed ratio λ is varied to assess its impact on material removal depth uniformity, while the spindle speed is set constant for stable automatic polishing. The influence of various parameters is explored in the polishing process simulation, demonstrating the validity of the proposed APFRS, and providing an effective approach to accelerating the progress of automatic polishing.

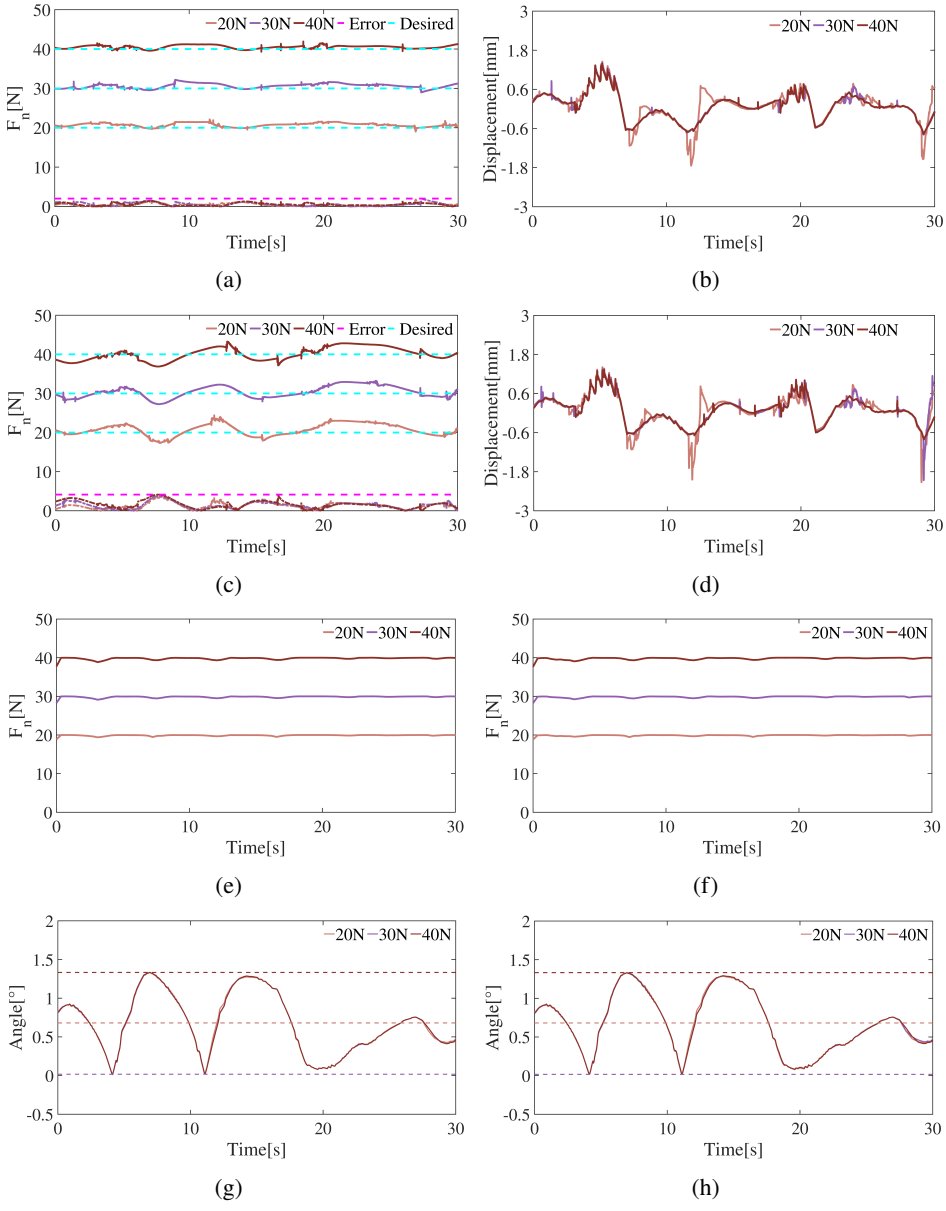

Fig. 13. Normal polishing force errors (a) and (c), telescoping displacement (b) and (d), regulated polishing force (e) and (f), angle error (g) and (h) under admittance controller and PID controller with 20 N, 30 N, 40 N as the reference force

5. Conclusions

This study introduces a new approach to robotic polishing through a novel online trajectory generator that eliminates the reliance on pre-defined CAD models for free-form surfaces. By integrating a friction-compensated surface normal estimator with a modified Preston material removal model, our proposed model-predictive adaptive parameters fusion regulation strategy (APFRS) enables precise, real-time trajectory optimization and adaptive control of polishing parameters, including normal force and feed rate. Through systematic investigation with the use of a virtual robotic polishing system equipped with a compliant end-effector and a normal force controller, we developed a posture/position estimator that accounts for reaction forces and friction in disc-workpiece interactions. The modified material removal rate (MRR) distribution further elucidates how contact forces influence material removal depth, enhancing process accuracy. The simulation results show the effectiveness of APFRS in the polishing process, with the maximum predicted angle error of the surface normal estimator ranging from 0.01° to 1.33°, and a maximum normal polishing force error of only 1.9 N, with a mean error of 0.53 N.

These findings demonstrate significant consistency and precision in the normal approach for polishing workpiece with unknown geometric data, ensuring a high automation level in polishing application. Furthermore, the simulation using the disc tool substantiates the efficacy of our control methodology. This research provides valuable insights into optimizing automated polishing procedures, providing a feasible approach for advancements in manufacturing practices within the industries which require precision surface finishing. Future work may explore additional parameters and practical applications, enhancing the versatility and resilience of automated polishing systems.

Acknowledgements

We appreciate support for the research from the National Natural Science Foundation of China (Grant No. 52275005), the Natural Science Basic Research Program of Shaanxi (Grant Nos. 2025JC-QYXQ-027, 2025JC-YBMS-619 and No. 2022JQ-342), the Fundamental Research Funds for the Central Universities, CHD (Grant No. 300102253201), the Open Research Fund of Anhui Province Key Laboratory of Machine Vision Detection and Perception (Grant No. KLMVI-2025-HIT-06), and the China Postdoctoral Science Foundation (Grant No. 2024M760002).

References

[1] Wei Ji and Lihui Wang. Industrial robotic machining: a review. *The International Journal of Advanced Manufacturing Technology*, 103:1239–1255, 2019. doi: 10.1007/s00170-019-03403-z.

[2] Wu-Le Zhu and Anthony Beaucamp. Compliant grinding and polishing: A review. *International Journal of Machine Tools and Manufacture*, 158:103634, 2020. doi: 10.1016/j.ijmachtools.2020.103634.

[3] Dahu Zhu, Xiaozhi Feng, Xiaohu Xu, Zeyuan Yang, Wenlong Li, Sijie Yan, and Han Ding. Robotic grinding of complex components: a step towards efficient and intelligent machining–challenges, solutions, and applications. *Robotics and Computer-Integrated Manufacturing*, 65:101908, 2020. doi: 10.1016/j.rcim.2019.101908.

[4] Thomas Weingartshofer, Bernhard Bischof, Martin Meiringer, Christian Hartl-Nesic, and Andreas Kugi. Optimization-based path planning framework for industrial manufacturing processes with complex continuous paths. *Robotics and Computer-Integrated Manufacturing*, 82:102516, 2023. doi: 10.1016/j.rcim.2022.102516.

[5] Linqiang Gong, Cheng Fan, Zhi Shen, Zhang Chen, and Lei Zhang. Research on discretization algorithm of free-form surface for robotic polishing. *Journal of Manufacturing Processes*, 92:350–370, 2023. doi: 10.1016/j.jmapro.2023.02.040.

[6] Yanjun Han, Chong Wang, Haiyang Zhang, Menghuan Yu, Xunchuan Chang, Jie Dong, and Yunfei Zhang. Adaptive polishing path optimization for free-form uniform polishing based on footprint evolution. *The International Journal of Advanced Manufacturing Technology*, 130(9):4311–4324, 2024. doi: 10.1007/s00170-024-12996-z.

[7] Ercan Oztemel and Samet Gursev. Literature review of industry 4.0 and related technologies. *Journal of Intelligent Manufacturing*, 31:127–182, 2020. doi: 10.1007/s10845-018-1433-8.

[8] Kaichao Ma and Guilin Yang. Kinematic design of a 3-DOF force-controlled end-effector module. In *2016 IEEE 11th Conference on Industrial Electronics and Applications (ICIEA)*, pages 1084–1089, 2016. doi: 10.1109/ICIEA.2016.7603743.

[9] Alexander Verl, Anna Valente, Shreyes Melkote, Christian Brecher, Erdem Ozturk, and Lutfi Taner Tunc. Robots in machining. *CIRP Annals*, 68(2):799–822, 2019. doi: 10.1016/j.cirp.2019.05.009.

[10] Tie Zhang, Meng Xiao, Yan-biao Zou, Jia-dong Xiao, and Shou-yan Chen. Robotic curved surface tracking with a neural network for angle identification and constant force control based on reinforcement learning. *International Journal of Precision Engineering and Manufacturing*, 21:869–882, 2020. doi: 10.1007/s12541-020-00315-x.

[11] Hélio Ochoa and Rui Cortesão. Impedance control architecture for robotic-assisted mold polishing based on human demonstration. *IEEE Transactions on Industrial Electronics*, 69(4):3822–3830, 2021. doi: 10.1109/TIE.2021.3073310.

[12] Srinivasan Lakshminarayanan, Sreekanth Kana, Dhanya Menoth Mohan, Omey Mohan Manyar, David Then, and Domenico Campolo. An adaptive framework for robotic polishing based on impedance control. *The International Journal of Advanced Manufacturing Technology*, 112(1):401–417, 2021. doi: 10.1007/s00170-020-06270-1.

[13] Jorge Borrell, Alejandra González, Carlos Perez-Vidal, Luis Gracia, and J Ernesto Solanes. Cooperative human–robot polishing for the task of patina growing on high-quality leather shoes. *The International Journal of Advanced Manufacturing Technology*, 125(5):2467–2484, 2023. doi: 10.1007/s00170-022-10620-6.

[14] Alejandra González, Carlos Perez-Vidal, Jorge Borrell, J. Ernesto Solanes, and Luis Gracia. Development of a collaborative robotic system to polish leather surfaces. *International Journal of Computer Integrated Manufacturing*, 37(3):285–303, 2024. doi: 10.1080/0951192X.2023.2209874.

[15] Jian Li, Yisheng Guan, Haowen Chen, Bing Wang, and Tao Zhang. Robotic polishing of unknown-model workpieces with constant normal contact force control. *IEEE/ASME Transactions on Mechatronics*, 28(2):1093–1103, 2023. doi: 10.1109/TMECH.2022.3216314.

[16] Xinqing Wang, Xin Wang, Zhenyu Yang, and Yupeng Zou. An investigation of real-time robotic polishing motion planning using a dynamical system. *Machines*, 12(4):278, 2024. doi: 10.3390/machines12040278.

[17] Dingwei Li, Jixiang Yang, Huan Zhao, and Han Ding. Contact force plan and control of robotic grinding towards ensuring contour accuracy of curved surfaces. *International Journal of Mechanical Sciences*, 227:107449, 2022. doi: 10.1016/j.ijmecsci.2022.107449.

[18] MuBang Xiao, Ye Ding, Zaojun Fang, and Guilin Yang. Contact force modeling and analysis for robotic tilted-disc polishing of freeform workpieces. *Precision Engineering*, 66:188–200, 2020. doi: 10.1016/j.precisioneng.2020.04.019.

[19] Stefan Schneyer, Arne Sachtler, Thomas Eiband, and Korbinian Nottensteiner. Segmentation and coverage planning of freeform geometries for robotic surface finishing. *IEEE Robotics and Automation Letters*, 8(8):5267–5274, 2023. doi: 10.1109/LRA.2023.3293309.

[20] Loris Roveda and Marco Pavone. Gradient descent-based task-orientation robot control enhanced with Gaussian process predictions. *IEEE Robotics and Automation Letters*, 2024. doi: 10.1109/LRA.2024.3438039.

[21] Alessandra Tafuro, Carla Ghalloub, Andrea Maria Zanchettin, and Paolo Rocco. Autonomous robotic polishing of free-form poly-surfaces: planning from scanning in realistic industrial setting. *Procedia Computer Science*, 232:2488–2497, 2024. doi: 10.1016/j.procs.2024.02.145.

[22] R. Kankaanranta and H. Koivo. A model for constrained motion of a serial link manipulator. In *Proceedings. 1986 IEEE International Conference on Robotics and Automation*, volume 3, pages 1186–1191. IEEE, 1986. doi: 10.1109/ROBOT.1986.1087571.

[23] Di Xiao, Bijoy K Ghosh, Ning Xi, and Tzyh Jong Tarn. Sensor-based hybrid position/force control of a robot manipulator in an uncalibrated environment. *IEEE Transactions on Control Systems Technology*, 8(4):635–645, 2000. doi: 10.1109/87.852909.

[24] Chien-Chern Cheah, Sadao Kawamura, and Suguru Arimoto. Stability of hybrid position and force control for robotic manipulator with kinematics and dynamics uncertainties. *Automatica*, 39(5):847–855, 2003. doi: 10.1016/S0005-1098(03)00002-5.

[25] Mehrzad Namvar and Farhad Aghili. Adaptive force-motion control of coordinated robots interacting with geometrically unknown environments. *IEEE Transactions on Robotics*, 21(4):678–694, 2005. doi: 10.1109/TRO.2004.842346.

[26] Yiannis Karayiannidis and Zoe Doulgeri. Adaptive control of robot contact tasks with on-line learning of planar surfaces. *Automatica*, 45(10):2374–2382, 2009. doi: 10.1016/j.automatica.2009.06.023.

[27] Yiannis Karayiannidis, Christian Smith, Francisco E Vina, and Danica Kragic. Online contact point estimation for uncalibrated tool use. In *2014 IEEE International Conference on Robotics and Automation (ICRA)*, pages 2488–2494. IEEE, 2014. doi: 10.1109/ICRA.2014.6907206.

[28] Yuta Oba and Yasuhiro Kakinuma. Simultaneous tool posture and polishing force control of unknown curved surface using serial-parallel mechanism polishing machine. *Precision Engineering*, 49:24–32, 2017. doi: 10.1016/j.precisioneng.2017.01.006.

[29] Anton Royanto Ahmad, Chyi-Yeu Lin, Syed Humayoon Shah, and Yong-Sheng Cheng. Design of a compliant robotic end-effector tool for normal contact estimation. *IEEE Sensors Journal*, 23(2):1515–1526, 2022. doi: 10.1109/JSEN.2022.3226492.

[30] Jian Li, Yisheng Guan, Haowen Chen, Bing Wang, Tao Zhang, Jie Hong, and Danwei Wang. Real-time normal contact force control for robotic surface processing of workpieces without a priori geometric model. *The International Journal of Advanced Manufacturing Technology*, 119:2537–2551, 2022. doi: 10.1007/s00170-021-07497-2.

[31] Jixiang Yang, Haiqing Chen, Ruibin Qi, Han Ding, and Yuehong Yin. A novel approach to robotic grinding guaranteeing profile accuracy using rigid-flexible coupling force control for free-formed surfaces. *CIRP Annals*, 72(1):313–316, 2023. doi: 10.1016/j.cirp.2023.04.069.

[32] Wu-Le Zhu, Yue Yang, Hao Nan Li, Dragos Axinte, and Anthony Beaucamp. Theoretical and experimental investigation of material removal mechanism in compliant shape adaptive grinding process. *International Journal of Machine Tools and Manufacture*, 142:76–97, 2019. doi: 10.1016/j.ijmachtools.2019.04.011.

[33] Chunyan Wang, Guicheng Wang, Chungen Shen, and Xinyu Dai. Multi-objective optimization of surface integrity in the grind-hardening process. *Coatings*, 14(7):910, 2024. doi: 10.3390/coatings14070910.

[34] Yasuhiro Kakinuma, Keisuke Igarashi, Seiichiro Katsura, and Tojiro Aoyama. Development of 5-axis polishing machine capable of simultaneous trajectory, posture, and force control. *CIRP Annals*, 62(1):379–382, 2013. doi: 10.1016/j.cirp.2013.03.135.

[35] Cheng Fan, Ji Zhao, Lei Zhang, Yoke San Wong, Geok Soon Hong, and Wansong Zhou. Modeling and analysis of the material removal profile for free abrasive polishing with sub-aperture pad. *Journal of Materials Processing Technology*, 214(2):285–294, 2014. doi: 10.1016/j.jmatprotec.2013.09.010.

[36] Fengjie Tian, Chong Lv, Zhenguo Li, and Guangbao Liu. Modeling and control of robotic automatic polishing for curved surfaces. *CIRP Journal of Manufacturing Science and Technology*, 14:55–64, 2016. doi: 10.1016/j.cirpj.2016.05.010.

[37] Peng Xu, Bing Li, Chi-Fai Cheung, and Ju-Fan Zhang. Stiffness modeling and optimization of a 3-DOF parallel robot in a serial-parallel polishing machine. *International Journal of Precision Engineering and Manufacturing*, 18:497–507, 2017. doi: 10.1007/s12541-017-0060-1.

[38] Tie Zhang, Meng Xiao, Yan-biao Zou, Jia-dong Xiao, and Shou-yan Chen. Robotic curved surface tracking with a neural network for angle identification and constant force control based on reinforcement learning. *International Journal of Precision Engineering and Manufacturing*, 21:869–882, 2020. doi: 10.1007/s12541-020-00315-x.

[39] Tsuneo Yoshikawa and Akio Sudou. Dynamic hybrid position/force control of robot manipulators-on-line estimation of unknown constraint. *IEEE Transactions on Robotics and Automation*, 9(2):220–226, 1993. doi: 10.1109/70.238286.

[40] Guirong Wang, Fei Xu, Kun Zhou, and Zhihui Pang. S-velocity profile of industrial robot based on nurbs curve and slerp interpolation. *Processes*, 10(11):2195, 2022. doi: 10.3390/pr10112195.

[41] MB Peterson. Design considerations for effective wear control. *Wear Control Handbook*, pages 413–474, 1980.

[42] Xinsheng He, Hongkai Jin, Chongqiu Zhou, Chunfu Gao, Guang Zhang, and E Shiju. Modeling of material removal in magnetic finishing based on maxwell's stress tensor theory and its experimental validation. *Journal of Materials Processing Technology*, 312:117808, 2023. doi: 10.1016/j.jmatprotec.2022.117808.

[43] Fengjie Tian, Zhenguo Li, Chong Lv, and Guangbao Liu. Polishing pressure investigations of robot automatic polishing on curved surfaces. *The International Journal of Advanced Manufacturing Technology*, 87:639–646, 2016. doi: 10.1007/s00170-016-8527-2.